SCIENTIFIC REPORTS

OPEN

SUBJECT AREAS:
OPTICAL IMAGING
FLUORESCENT PROTEINS

Received
16 September 2013

Accepted
15 January 2014

Published
3 February 2014

Correspondence and requests for materials should be addressed to L.V.W. (lhwang@biomed.wustl.edu) or V.V.V. (vladislav.verkhusha@einstein.yu.edu)

* These authors contributed equally to this work.

Multicontrast photoacoustic *in vivo* imaging using near-infrared fluorescent proteins

Arie Krumholz[1]*, Daria M. Shcherbakova[2]*, Jun Xia[1], Lihong V. Wang[1] & Vladislav V. Verkhusha[2]

[1]Department of Biomedical Engineering, Optical Imaging Laboratory, Washington University in St. Louis, St. Louis, MO 63130, USA, [2]Department of Anatomy and Structural Biology, and Gruss-Lipper Biophotonics Center, Albert Einstein College of Medicine, Bronx, NY 10461, USA.

Non-invasive imaging of biological processes *in vivo* is invaluable in advancing biology. Photoacoustic tomography is a scalable imaging technique that provides higher resolution at greater depths in tissue than achievable by purely optical methods. Here we report the application of two spectrally distinct near-infrared fluorescent proteins, iRFP670 and iRFP720, engineered from bacterial phytochromes, as photoacoustic contrast agents. iRFPs provide tissue-specific contrast without the need for delivery of any additional substances. Compared to conventional GFP-like red-shifted fluorescent proteins, iRFP670 and iRFP720 demonstrate stronger photoacoustic signals at longer wavelengths, and can be spectrally resolved from each other and hemoglobin. We simultaneously visualized two differently labeled tumors, one with iRFP670 and the other with iRFP720, as well as blood vessels. We acquired images of a mouse as 2D sections of a whole animal, and as localized 3D volumetric images with high contrast and sub-millimeter resolution at depths up to 8 mm. Our results suggest iRFPs are genetically-encoded probes of choice for simultaneous photoacoustic imaging of several tissues or processes *in vivo*.

Photoacoustic (PA) tomography is an emerging technology that can produce images of living objects at multiple scales, ranging from organelles to organs[1]. In contrast to purely optical methods[2], such as fluorescence imaging and bioluminescence imaging, photoacoustic tomography (PAT) can achieve good spatial resolution at depths of more than 1 mm inside scattering biological tissue[1,3]. Based on the photoacoustic effect, PAT detects thermoelastically induced ultrasonic waves as a result of light absorption by biomolecules. Ultrasonic waves are scattered much less than photons in tissue. This enables PAT to be used for high resolution imaging deep in tissue. In PAT, the spatial resolution scales with the imaging depth depending on the application, while still maintaining a high depth-to-resolution ratio[4]. Various endogenous and exogenous absorbers can serve as PAT contrast agents, enabling the visualization of vasculature, blood oxygenation levels, biomarkers and gene expression[3]. The primary endogenous absorbers are DNA/RNA, hemoglobin, melanin, water, and lipid. Exogenous contrast agents including organic dyes, nanoparticles, and reporter genes, extend the applications of PAT to molecular imaging.

The application of genetically encoded contrast agents in PAT is a powerful approach for *in vivo* deep-tissue monitoring of specific genetically defined cell populations with good spatial resolution[5]. Compared with dyes and nanoparticles, genetically encoded probes have several advantages. First, the labeling is specific to the transfected cell population. Second, reporter genes avoid some difficulties associated with targeted delivery, particularly non-specific accumulation and clearance from the body. Strong light absorbing fluorescent proteins (FPs)[6,7] with low and moderate quantum yields provide excellent contrast for PAT[3]. EGFP, DsRed, and mCherry have been applied to imaging of small transparent organisms such as zebrafish and fruit fly pupa[8]. For deep-tissue PAT, probes absorbing in the near-infrared (NIR) spectral range are desirable. In the NIR optical window of 650–900 nm, absorption by hemoglobin and water is low, making probes absorbing within this range particularly useful[9]. Although several far-red GFP-like FPs such as mNeptune[10], E2-Crimson[11], eqFP670[12], TagRFP657[13] and TagRFP675[14] have been available, and their utility for *in vivo* imaging was demonstrated, their absorption was not in the NIR optical window[7]. Bacterial phytochromes are promising templates to engineer NIR FPs, NIR reporters[15] and NIR optogenetic tools[16]. One NIR FP of this type, called iRFP713 (aka iRFP)[17], was visualized by using PAT in mice[18]. iRFP713 was also used as a contrast agent for non-invasive detection of *in vivo* circulating tumor cells by a combined PA and fluorescence flow cytometry approach[19].

Imaging multiple contrast agents in PAT can provide essential information about complex physiological and pathogenic processes in living organisms, such as the interaction of a tumor with its microenvironment. At least two different NIR genetically encoded probes are required for imaging more than one specifically defined cell population inside living mammals. Until now, spectrally distinct NIR FPs designed for this purpose have not been available. Additionally, the simultaneous imaging of multiple genetically encoded contrast agents has never before been demonstrated with PAT. Recently developed iRFP670 (absorption/emission maxima at 645 nm/670 nm)[20] and iRFP720 (absorption/emission maxima at 703 nm/720 nm)[20] FPs, engineered on the basis of two different bacterial phytochromes, are good candidates for multicontrast PAT. These proteins have high affinity for and incorporate endogenous biliverdin, which is abundant in mammalian tissues, as a chromophore. As they do not require any exogenous supplements to be added, these FPs can be used as easily as conventional GFP-like FPs. Expression of these proteins and closely related iRFP713 in different types of mammalian cells and tissues, such as various human cells, rat cells, mouse liver and mouse spleen, have been reported[10,13]. Both iRFP670 and iRFP720 proteins have high extinction coefficients and relatively low fluorescence quantum yields (Table 1), which are favorable properties of PA contrast agents, as PA signals are proportional to the product of the molar extinction coefficient and the nonradiative quantum yield[3]. Because the two iRFPs are spectrally distinct and both absorb in the NIR optical window (Figure 1a), we can separate the contribution to the signal of each iRFP from that of each other and of hemoglobin.

Results

Characterization of iRFP670 and iRFP720 as probes for multicontrast PAT. To verify that iRFP670 and iRFP720 are indeed the best available candidates for simultaneous deep-tissue imaging in PAT, we compared PA signals of purified iRFP670, iRFP720, iRFP713, and other available far-red shifted fluorescent proteins including mNeptune, E2-Crimson and eqFP670 (Table 1). Hemoglobin from lysed blood was used as the reference standard. The purified FPs diluted to equal concentrations were imaged using a PA computed tomography (PACT) setup[21] (Figure 1b) at four different laser wavelengths spanning the spectral region of the FPs' absorption (600 nm, 645 nm, 680 nm and 715 nm). The amplitudes of the PACT signals from FPs were normalized to the signal from blood at 600 nm. The values (Figure 1c) show that all FPs engineered from bacterial phytochromes (iRFP670, iRFP713 and iRFP720), with absorption maxima in the NIR optical window, produced signals more than 2-fold higher than blood at wavelengths above 600 nm. These protein's favorable spectra make them more suitable for simultaneous detection with hemoglobin than the other tested far-red FPs. Figure 1c also demonstrates that two wavelengths, 645 nm and 715 nm, can be used to separate the signals of iRFP670 and iRFP720, from each other and from the blood signal. At 645 nm, the signal of iRFP670 is nearly twice that of iRFP720, whereas at 715 nm, the signal of iRFP670 is almost negligible. This corresponds well with the spectral overlay. To estimate the contrast between proteins, we quantified the ratios of the signals of pairs of FPs at two wavelengths. The ratio between iRFP670 and iRFP720 signals at 645 nm and 715 nm is 11-fold, while for iRFP713 and iRFP720 at these wavelengths it is 4.3-fold, and for iRFP670 and iRFP713 at 645 nm and 680 nm it equals to 2.9-fold. These data support the choice of iRFP670 and iRFP720 for multicontrast PAT.

From the above discussion, four wavelengths (645 nm, 715 nm, 750 nm and 800 nm) were selected for multicontrast PA imaging of iRFP670 and iRFP720, and hemoglobin; the first two wavelengths correspond to the absorption peaks of iRFP670 and iRFP720. 750 nm and 800 nm were chosen due to the negligible absorption from the proteins while relatively high hemoglobin absorption was maintained. This combination enabled separate detection of two FPs, and hemoglobin-form lysed blood, not only on the surface but also at depths up to 1.9 cm of chicken breast tissue (Figure 1d). The contribution by each absorber to the signal was estimated using a least squares algorithm. In this method, the signal is modeled as a linear combination of signals from each absorber, and the weight of each absorber to the signal is determined by its molar extinction coefficient. The intrinsic advantage of the PACT's setup to penetrate deep in tissue[1], combined with the NIR-shifted absorption, allowed detection at such a depth. Due to the differences in illumination schemes between the *in vitro* and *in vivo* experiments, the noise equivalent concentration (NEC) was not calculated for this system as the sensitivity is correlated with the illumination intensity. However, the *in vitro* results show that despite strong attenuation of the illumination, the proteins are still separable spectrally from each other and from blood.

Next we estimated the applicability of iRFP670 and iRFP720 in a deep PA macroscopy (deep-PAMac) imaging setup[22]. Compared with PACT, deep-PAMac (which is an acoustic-resolution PAT implementation) images less deeply but can produce a depth-resolved top-down cross-section, which can then be raster scanned to produce a volumetric image. Figure 2a is a schematic of the setup. Compared to whole-body PACT, deep-PAMac has the additional advantage of allowing the stacking of tissue to simulate depth while maintaining the same geometry. To test the applicability of the iRFPs for multicontrast deep-PAMac, we imaged protein samples of iRFP670, iRFP720, and whole blood, without and with a tissue overlay of 5.0 mm to simulate depth (Figure 2b). To analyze the sensitivity of the iRFPs' detection deep in tissue, we calculated the NECs. For both proteins the NEC values at the optimal excitation wavelengths (645 nm for iRFP670 and 715 nm for iRFP720) were more than one order of magnitude lower than for the blood (Figure 2c). We estimated the ratio of signals between iRFP670 and iRFP720 at 645 nm and 715 nm to be 10-fold, close to what we observed in PACT. Also as in PACT, the proteins (32 μM of each FP) and the blood (2.3 mM concentration of hemoglobin) could be separated using the four wavelengths (Figure 2b).

Application of iRFP670 and iRFP720 to *in vivo* PAT. After the *in vitro* experiments, we tested the performance of iRFP670 and iRFP720 in simultaneous deep-tissue imaging *in vivo*. We employed a mouse xenograft breast cancer model[23]. As contrast agents, FPs allow for

Table 1 | Optical properties of the far-red and near-infrared fluorescent proteins used in the study

FPs	Absorption maximum (nm)	Excitation maximum (nm)	Emission maximum (nm)	Molar extinction coefficient (M^{-1} cm^{-1})	Quantum yield of fluorescence	Molar extinction coefficient × Non-radiative quantum yield (M^{-1} cm^{-1})
mNeptune	600	600	650	59,000	0.20	47,200
E2-Crimson	603	605	646	58,500	0.12	51,480
eqFP670	603	605	670	70,000	0.06	65,800
iRFP713	692	690	713	98,000	0.06	92,120
iRFP670	645	643	670	114,000	0.11	101,460
iRFP720	703	702	720	96,000	0.06	90,240

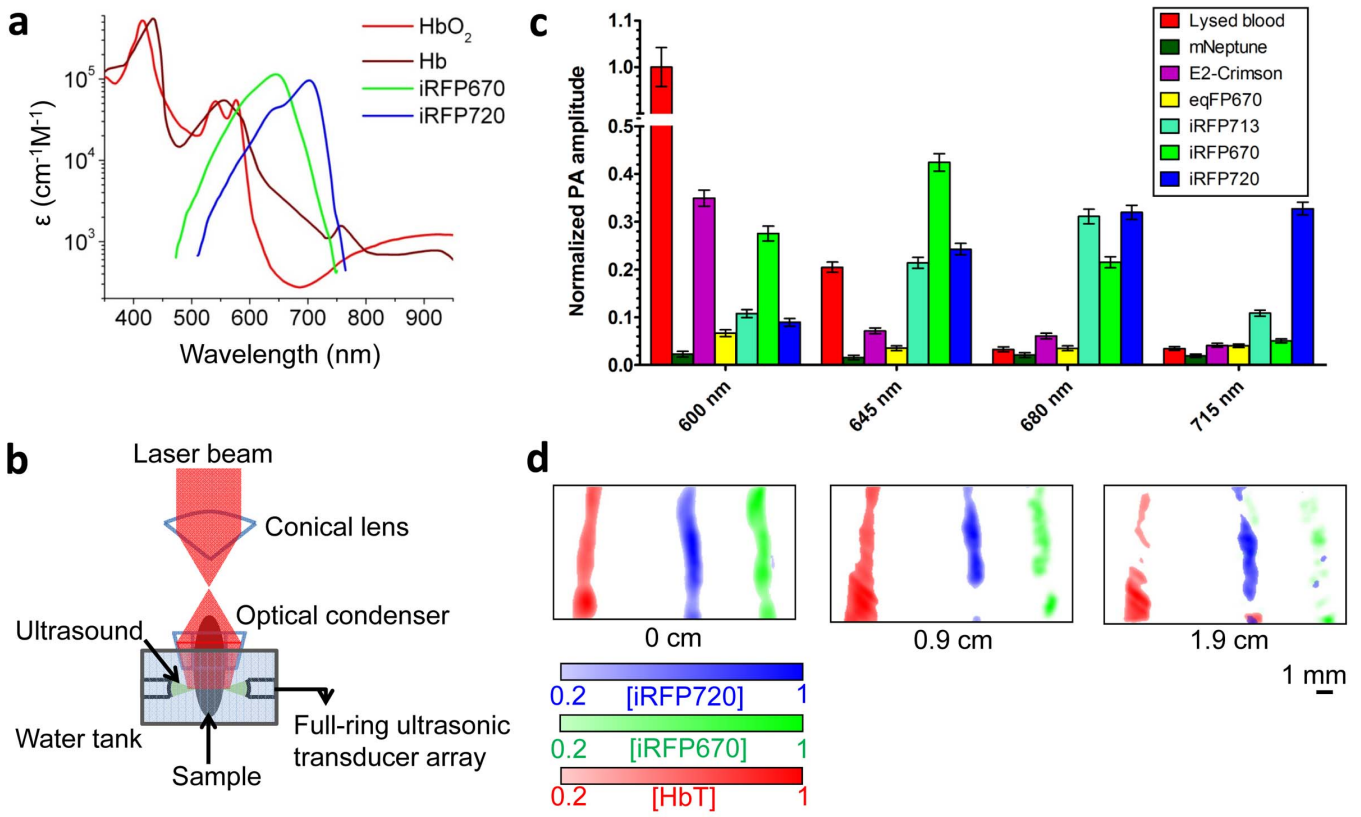

Figure 1 | Photoacoustic properties of purified iRFP670 and iRFP720 proteins. (a) Overlay of the molar extinction spectra of iRFP670, iRFP720, oxygenated hemoglobin (HbO_2) and deoxygenated hemoglobin (Hb). (b) Illumination and detection scheme for PACT. (c) Photoacoustic signal amplitudes of equal amounts of purified FPs (mNeptune, E2-Crimson, eqRFP670, iRFP670, iRFP713, iRFP720) at the four indicated wavelengths. Lysed bovine blood was used as a reference standard. The values were normalized to blood signal at 600 nm. (d) PACT images of tubes containing lysed blood and equal concentrations of purified iRFP670 and iRFP720. Total hemoglobin (HbT) (in red), iRFP670 (in green) and iRFP720 (in blue) signals were detected and unmixed at different depths (0, 0.9 and 1.9 mm) of overlaid tissue. Scale bar, 1 mm.

analysis of labeled cells and tissues by conventional fluorescent techniques, such as microscopy, flow cytometry, and whole-body imaging. To select for stably expressing rat adenocarcinoma MTLn3 cells for tumor implantation, preclonal mixtures were selected by fluorescence activated cell sorting (FACS). The selected cells expressing iRFP670 and iRFP720 were analyzed by microscopy (Figure 3a), and are distinguishable from each other by flow cytometry (Figure 3b). To demonstrate that iRFP670 and iRFP720 can be used simultaneously and separated from blood signal *in vivo*, mice were co-injected with two types of MTLn3 cells (expressing either iRFP670 or iRFP720) causing two tumors to grow spatially close to each other. Three weeks after the injection, the tumors were easily separated from each other by whole-body epifluorescence imaging in two filter channels, using a standard IVIS Spectrum imaging system (Figure 3c).

At the same time, we imaged the mice with the two tumors by PACT. The circular-array PACT shown schematically in Figure 1b is designed to accommodate cylindrical objects, such as the mouse trunk[24]. The extensive imaging depth of this setup provides 2D cross-sections of a whole mouse body with 0.1 mm in-plane resolution[18]. A representative mouse with the two implanted tumors (Figure 4a) was imaged at all four wavelengths (Figure 4b). The combined image with unmixed signals overlaid (Figure 4c) shows both the iRFP670 and iRFP720 expressing tumors and major blood vessels in a cross-section of the mouse body (see also Supplementary Figures S1 and S2 online).

Further, we applied the deep-PAMac setup to the same mice to study the tumors in more detail. The deep-PAMac, utilized with a 10 MHz center frequency focused transducer, can achieve good resolution (280 μm lateral, 75 μm axial) at depths up to a few millimeters and, due to the setup geometry, gain the ability to simulate depth by overlaying additional biological tissue on the sample[18,25]. The results show detailed images of the tumors and surrounding vessels at depths of up to 8 mm inside the mouse body (Figure 5a). Two orthogonal maximum amplitude projection images per each of four wavelengths show different spectral dependence of the signals from the tumors and from the surrounding tissue, thus allowing spectral separation. The spatial locations of the two tumors and blood are detectable even at depths up to 5 mm under overlaid biological tissue (Figure 5b). Although the signal to noise ratio is low, the spectral differences between the absorbers allowed discriminating between regions. The wavelength dependent attenuation of the incident light can lead to inaccuracies in the quantitative values obtained; however, the spectra of the absorbers are different enough to discriminate the locations of the absorbers. This demonstrates the ability to separate image contributions of iRFP670, iRFP720, and hemoglobin noninvasively in one subject (combined pseudocolor images in Figure 5). The differences in a scale between the proteins could be due to variation in expression. We quantified the PA signals from tumors and blood and estimated the concentration of the iRFPs to be between 16–30 μM.

Discussion

PAT is a promising technique for visualizing biological processes deep inside tissues. In this paper we demonstrated that PAT can be utilized to simultaneously and noninvasively image two differently labeled tumors and blood vessels *in vivo*. This is the first demonstration of

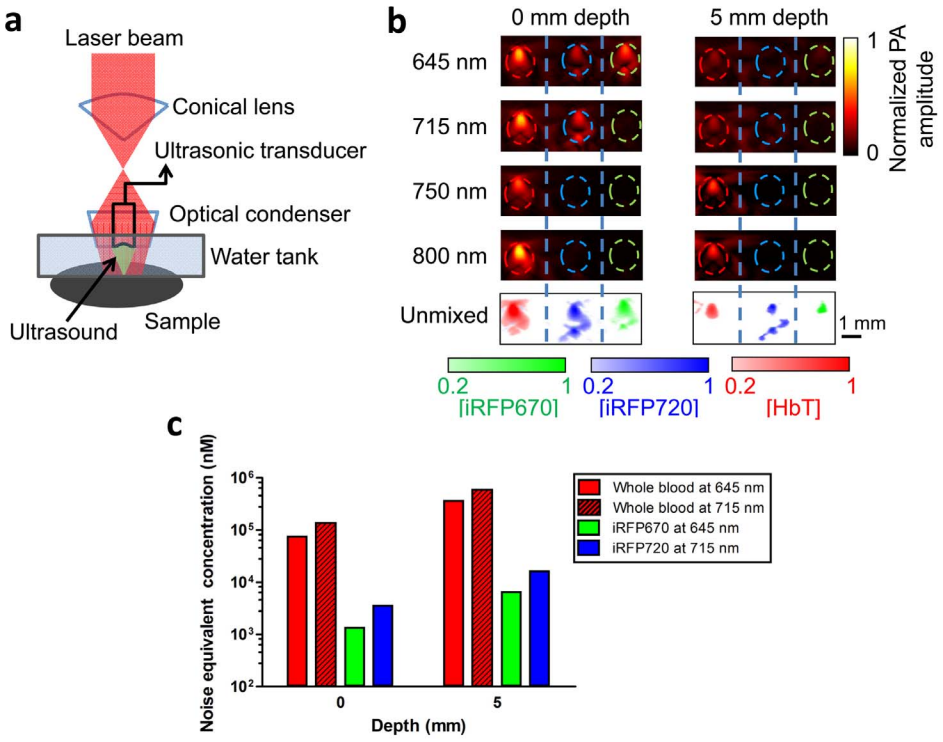

Figure 2 | Deep-PAMac characterization of iRFP670 and iRFP720 proteins in phantom. (a) Illumination and detection scheme for deep-PAMac. (b) Deep-PAMac cross-sections of the tubes containing whole blood (left, in red), iRFP720 (center, in blue) and iRFP670 (right, in green) at the four indicated wavelengths, without (left panel) and with (right panel) the overlaid tissue of 5 mm width. Dashed lines indicate the tube boundaries. Spectrally unmixed images of blood (HbT, in red), iRFP670 (in green) and iRFP720 (in blue) are shown at the bottom. (c) Calculated noise equivalent concentrations (NECs) for each of the purified proteins and total hemoglobin from blood at two depths (0 and 5 mm) mimicked by the tissue overlay. Scale bar, 1 mm.

PAT with two NIR genetically encoded probes and hemoglobin as the contrast agents in a living mouse.

We showed that, due to the NIR shifted spectra and sufficient spectral difference from each other, iRFP670 and iRFP720 are more suitable probes for *in vivo* PAT than conventional far-red GFP-like FPs. Use of GFP-like FPs for PA imaging of mammals is hindered by high hemoglobin absorption at wavelengths below 650 nm. In addition, chromophore formation in GFP-like FPs is oxygen-dependent. Since many tumors and pathogenic tissues are hypoxic, iRFP670 and iRFP720 are advantageous because the formation of their chromophores does not require oxygen. Furthermore, the NIR FPs exhibit good photoacoustic properties because of their high extinction coefficients and low fluorescence quantum yields, resulting in effective thermal relaxation and strong PA signals. Additionally, iRFP670 and iRFP720 have shown good photostability, which allows multiple optical exposures without altering the optical properties[13].

Genetically encoded iRFP670 and iRFP720 are produced by living cells and tissues, eliminating the need for delivery of contrast reagents

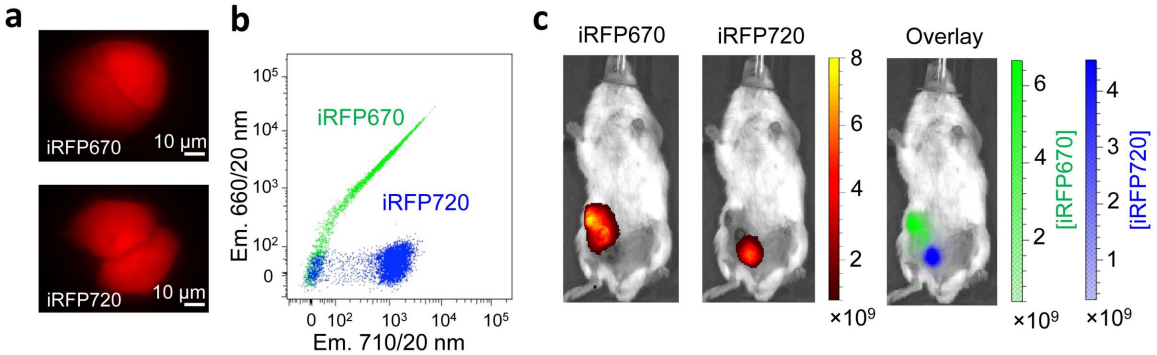

Figure 3 | Fluorescence imaging of MTLn3 cells in culture and in xenograft tumors. (a) Wide-field fluorescence microscopy of MTLn3 adenocarcinoma cells stably expressing iRFP670 or iRFP720. The filter combinations used were: 605/40 nm excitation and 640 long-pass for imaging of iRFP670, and 665/45 nm excitation and 725/50 nm emission for iRFP720. Scale bars, 10 μm. (b) Flow cytometry analysis of MTLn3 cells shown in (a). Cell fluorescence was excited with 635 nm laser and detected with a combination of two indicated emission filters. 10,000 events were analyzed for each cell type. (c) Representative fluorescence images of a living mouse with two tumors each expressing either iRFP670 (top tumor) or iRFP720 (bottom tumor). The images show the two channels with optimal fluorescence filters for iRFP670 (excitation 640/30 nm and emission 680/20 nm) and for iRFP720 (excitation 710/30 nm and emission 760/20 nm) and their overlay shown on the right. The images were obtained three weeks after cell injections. The color bars indicate the total fluorescent radiant efficiency in [p/s/cm^2/sr]/[μW/cm^2].

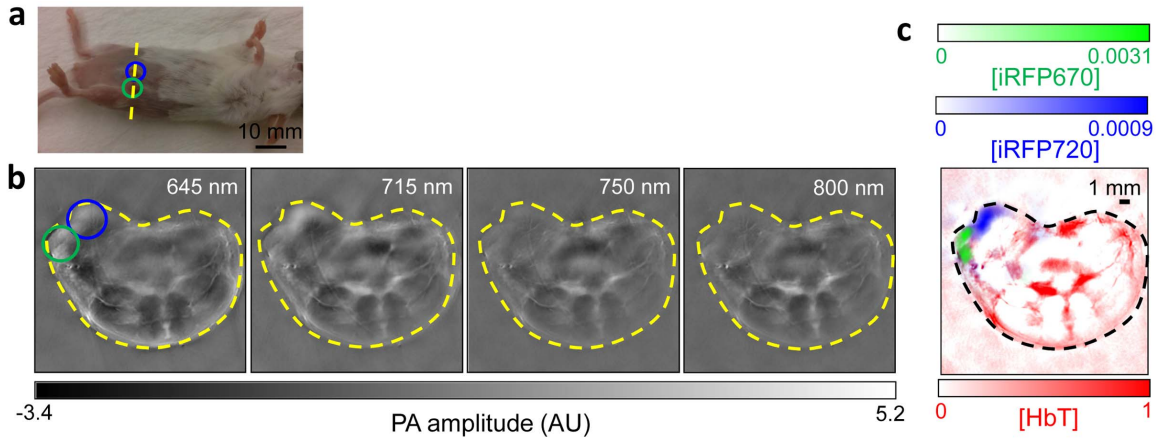

Figure 4 | PACT imaging of iRFP670 and iRFP720 in mouse tumor xenograft model. (a) Photograph of the mouse with iRFP670 (green circle) and iRFP720 (blue circle) expressing tumors growing in the mammary pads, three weeks after cell injection. The yellow line shows the approximate region of the imaged cross-section. The tumor regions are circled in blue and green. (b) PACT images of a mouse cross-section shown in (a) at four indicated wavelengths. (c) Spectrally separated image in pseudocolors (iRFP670 in green, iRFP720 in blue, total hemoglobin in red). The signals were normalized to the spectrally separated signal for blood. Dashed yellow and black lines show the mouse body borders. Scale bar, 1 mm.

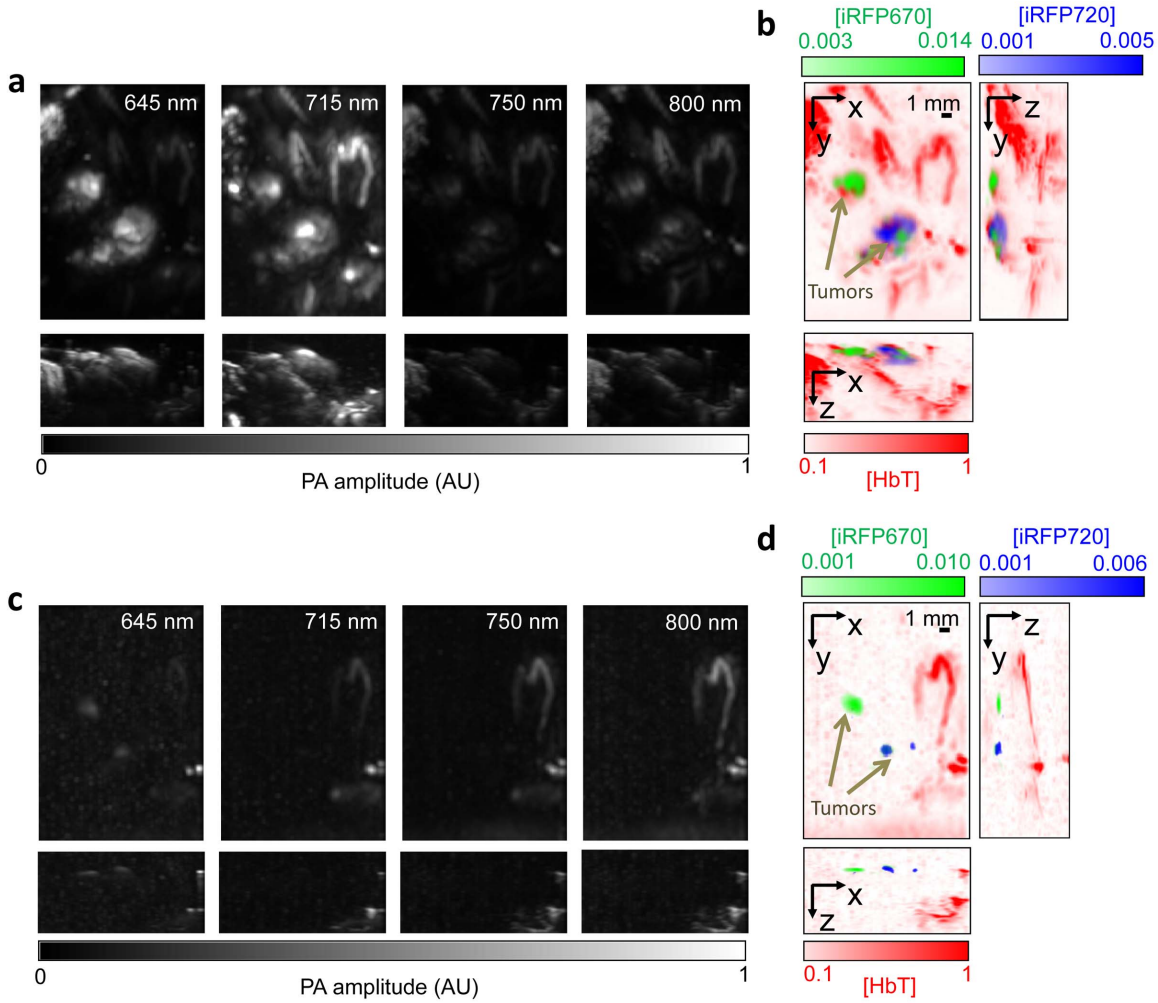

Figure 5 | Deep-PAMac imaging of iRFP670 and iRFP720 in mouse tumor xenograft model. Deep-PAMac maximum amplitude projection images of the tumors and surrounding major blood vessels taken with no overlaid tissue (a, b) and with 5 mm overlaid tissue (c, d) three weeks after cell injection. The four left images in panels (a, c) were acquired at the four indicated wavelengths. The pseudocolored images in panels (b, d) correspond to maximum amplitude projections with orthogonal orientations. The volumetric spectrally separated signals (iRFP670 in green, iRFP720 in blue, total hemoglobin in red) were normalized to the spectrally separated signal for blood. Positions of the tumors are indicated by the gray arrows.

such as organic dyes or nanoparticles. This property is advantageous for chronic monitoring of processes on a prolonged time scale. Moreover, the NIR FPs can be detected using conventional fluorescence modalities, which are easily accessible and provide additional information. Fluorescence *in vivo* imaging techniques, such as whole-body planar imaging and fluorescence molecular tomography (FMT)[26], complement PAT because they allow higher detection sensitivity, although at lower resolution than PAT. Lastly, iRFP670 and iRFP720 fluorescence allows additional postmortem detection of individual cells in histological sections or by using flow cytometry.

We took advantage of the scalability of PAT in different implementations and visualized iRFP670 and iRFP720 expressing tumors and hemoglobin at two scales. First, we imaged whole-mouse 2D sections with PACT, and second, we performed localized volumetric imaging of tumors inside the mouse body with deep-PAMac. The deep-PAMac approach provided both spectral resolution and maximum amplitude projections in three orthogonal planes. This combination resulted in spectrally resolved volumetric images, even at a depth of 5 mm, as mimicked by the overlaid tissue. Although photoacoustic imaging of single cells expressing FPs was demonstrated in cell culture[27], such a high sensitivity has not been shown in *in vivo* experiments. Using the presented setup, we were able to detect tumors of a millimeter size and larger inside of a living animal. Further optimization of the system's geometry and imaging setup will allow reaching the higher sensitivity *in vivo*, where the background absorption from blood and the intervening tissue between the absorbing cells and the surface of the body interfere with the detection.

In conclusion, multiple genetically-encoded contrast agents, such as iRFP670 and iRFP720 separated from hemoglobin, were imaged simultaneously deep *in vivo* using PAT. The future development and integration of various photoacoustic imaging approaches will advance studies of complex physiological and pathogenic processes for prolonged time periods in living animals at molecular and cellular levels. The presented technique holds great potential for both biological and preclinical studies on model organisms like mice. Although not applicable to humans, current progress in gene transfer technology[23] makes it possible to specifically label a variety of cells and organs *in vivo* in model animals. As compared to other optical methods, for example epifluorescence imaging, photoacoustic tomography achieves higher absorption-based contrast and visualizes more details because ultrasonic waves are scattered less than photons in tissue. Moreover, it provides additional information due to its ability to detect endogenous contrast agents, such as hemoglobin from blood. Multicontrast PAT, as the technique incorporating distinct NIR FPs demonstrated here, can be further applied to non-invasive detection of several processes including cancer growth, organ development, spread of infection, drug responses and gene activities in a living animal.

Methods

Protein expression and purification. Bacterial plasmids encoding mNeptune, E2-Crimson and eqFP670 with polyhistidine tags were provided by B. Glick (University of Chicago, USA), M. Lin (Stanford University, USA), and K. Lukyanov (Institute of Bioorganic Chemistry, Russia). Recombinant GFP-like FPs were expressed in LMG194 bacterial cells grown in RM medium supplemented with ampicillin, kanamycin, and 0.002% arabinose and then purified using a Ni-NTA agarose (Qiagen) according to the manufacture's protocol.

The iRFP670, iRFP713, and iRFP720 with polyhistidine tags on the N-terminus were expressed in LMG194 bacterial cells co-expressing heme oxygenase grown in RM medium supplemented with ampicillin, kanamycin, 0.002% arabinose, and 0.02% rhamnose. The NIR iRFPs were purified using Ni-NTA agarose and then washed in a buffer where imidazole was substituted for EDTA. All purified FP solutions were diluted to equal concentrations of 32 μM.

Photoacoustic studies of purified proteins. To determine the best FP for PA imaging, we constructed two phantoms consisting of approximately 40 mm long, 0.30 mm inner diameter (i.d.) tubing sections (Silastic) filled with one of the FP samples or lysed bovine blood. The tubes were then glued in parallel onto a flat gelatin block and imaged at 600 nm, 645 nm, 680 nm, and 715 nm, with approximately 90 mJ incident energy for the three lower wavelengths and 30 mJ incident energy at 715 nm. A 512-element ring transducer PACT system with top illumination from either an OPO laser (Vibrant 335I) or a Ti-Sapphite laser (LT-2211A) was used[21]. Both lasers were needed to cover the desired wavelength range. The wavelengths were chosen to cover wavelengths near the peak excitation of each of the FPs. The signal amplitude was corrected for laser energy at each wavelength using the average power reading from a power meter for normalization, and the signal from each of the FPs was further normalized to the signal of blood at 600 nm for comparison.

The depth analysis was performed on two phantoms consisting of approximately 15 mm long, 1.47 mm inner diameter tubing sections (Silastic) filled with iRFP670, iRFP720, or blood (lysed or whole) for comparison. The sections were then embedded in chicken breast tissue or glued onto a gelatin block and imaged using either the PACT or deep-PAMac setups, with illumination provided by the OPO or Ti-Sapphire laser[28]. Additional depths were simulated by stacking sections of chicken breast tissue on the sample surface. Twenty B-mode images were averaged at each depth. The noise equivalent concentration for each sample was calculated by dividing the known concentration of the absorber (32 μM for each FP and 2.3 mM for hemoglobin in the blood) by the signal-to-noise ratio in the region of the sample, and provided an estimate of the expected minimum concentration detectable by each system for this target.

Mammalian plasmids and cell culture. The plasmids used for expression of iRFP670 and iRFP720 in mammalian cells were based on pEGFP-N1 backbone (Clontech). The iRFP670 and iRFP720 genes were PCR-amplified as *Age*I-*Not*I fragments and swapped with the EGFP gene in pEGFP-N1 vector, thus generating the piRFP670 and piRFP720 plasmids.

A rat adenocarcinoma MTLn3 cell line was grown in αMEM medium (Life Technologies) containing 5% fetal bovine serum, 0.5% penicillin-streptomycin, and 2 mM glutamine. Plasmid transfections were performed using an Effectene reagent (Qiagen) according to the manufacturer's protocol. Stably expressing preclonal cell mixtures were selected with 700 μg/ml G418 antibiotic. Sorting of fluorescent cells was performed using a MoFlo XDP sorter (Beckman Coulter) equipped with a 676 nm Kr laser and a 700 nm long-pass emission filter.

Fluorescence imaging and flow cytometry. For fluorescence microscopy, cells were cultured in 35 mm glass bottom culture dishes with no. 1 cover glasses (MatTek). The MTLn3 cells expressing either iRFP670 or iRFP720 were imaged using an Olympus IX81 inverted epifluorescence microscope equipped with 200 W Me-Ha arc lamp (Lumen220Pro, Prior), a 100 × 1.4 numerical aperture oil immersion objective lens (UPlanSApo, Olympus), and two filter sets (one a 605/40 nm excitation, 667/30 nm emission and the other a 682/12 nm excitation, 721/42 nm emission). All filter sets were from Chroma. SlideBook v.4.1 software (Intelligent Imaging Innovations) was used to operate Olympus IX81 inverted microscope. Unmixed channels were pseudocolored and overlaid using the SlideBook v.4.1.

Discrimination between the two types of MTLn3 cells stably expressing iRFP670 and iRFP720 (one FP type per cell) was performed using a LSRII cytometer (BD Biosciences) equipped with a 635 nm laser and 660/20 nm and 710/20 nm emission filters. The obtained dot plots were superimposed. Flow cytometry calculations were performed using FlowJo software (Tree Star).

To implant xenograph tumors, approximately 10^6 MTLn3 cells stably expressing either iRFP670 or iRFP720 were injected into the mammary glands of female, 5–7 weeks old, SCID/NCr mice (Taconic), and imaged 3 weeks later using the IVIS Spectrum system (PerkinElmer/Caliper) in epifluorescence mode. Belly fur was removed using a depilatory cream. Mice were fed with AIN-93M Maintenance Purified Diet (TestDiet) to reduce their intrinsic autofluorescence level. All quantitative measurements of fluorescence signals were performed using Living Image v. 4.3.1 software (PerkinElmer/Caliper). To remove bleed-through of the excitation light into the emission channel, the software encoded adaptive background subtraction was performed.

Photoacoustic studies in mouse tumor xenograft model. For both PACT and deep-PAMac, approximately 10^6 MTLn3 cells stably expressing either iRFP670 or iRFP720 were injected into the mammary glands of four SCID/NCr mice. Three out of the four mice developed tumors which were photoacoustically detected two weeks later using PACT. For PACT, mice were imaged at the tumor region using four wavelengths, 645 nm, 715 nm, 750 nm, and 800 nm. For spectral separation, the images were then processed using a linear least-squares method for the four absorbers[8]. The model used is as follows:

$$PA = \varepsilon C,$$

where ε is a matrix of the extinction coefficients of each of the absorbers at each of the wavelengths, PA contains all the measurements per pixel at each wavelength, and C is the concentration of each absorber at each pixel. In this model we assume proper compensation for the incident light; however, for deeper imaging, the incident light attenuation is wavelength dependent and can lead to quantitative errors. We solve for C using a least squares solution:

$$\left(\varepsilon^T \varepsilon\right)^{-1} \varepsilon^T PA = C$$

The result is in relative values due to the unknown attenuation of light with depth.

For clear separation from blood, the wavelengths were chosen so that at least one wavelength was near the maximum absorption of each of the iRFP proteins, and light at other wavelengths was weakly absorbed.

For deep-PAMac, a 20 mm by 14 mm area was imaged. Images were taken at the same NIR wavelengths as in the PACT experiment, with depth simulated by stacking approximately 5 mm of chicken breast tissue over the sample. The same least-squares method was performed for spectral separation at both depths. To assess the iRFP670 and iRFP720 concentrations, we assumed the average total hemoglobin concentration to be similar through the depths imaged, and we normalized the calculated concentrations of iRFP670 and iRFP720 to the average total hemoglobin concentration at each depth. As noted previously, wavelength dependent attenuation of the incident light can lead to inaccuracies in the estimation of the concentration. Assuming that the illumination is similar per depth for the nearby blood vessels, and that the total hemoglobin concentration is 2.3 mM, we calibrate each of the proteins signal to the total hemoglobin signal at each depth. Consequently, the maximum iRFP670 and iRFP720 concentrations were estimated to be 16–30 μM.

All animal experiments were performed in AAALAC approved facilities using protocols approved either by the Albert Einstein College of Medicine Animal Usage Committee (fluorescence imaging) or by the Washington University in St. Louis Animal Use Committee (photoacoustic imaging).

1. Wang, L. V. & Hu, S. Photoacoustic tomography: in vivo imaging from organelles to organs. *Science* **335**, 1458–1462 (2012).
2. Ntziachristos, V. Going deeper than microscopy: the optical imaging frontier in biology. *Nat. Methods* **7**, 603–614 (2010).
3. Kim, C., Favazza, C. & Wang, L. V. In vivo photoacoustic tomography of chemicals: high-resolution functional and molecular optical imaging at new depths. *Chem Rev* **110**, 2756–2782 (2010).
4. Cai, X. *et al.* Multi-scale molecular photoacoustic tomography of gene expression. *PLoS One* **7**, e43999 (2012).
5. Li, L., Zemp, R. J., Lungu, G., Stoica, G. & Wang, L. V. Photoacoustic imaging of lacZ gene expression in vivo. *J Biomed Opt* **12**, 020504 (2007).
6. Piatkevich, K. D. & Verkhusha, V. V. Advances in engineering of fluorescent proteins and photoactivatable proteins with red emission. *Current opinion in chemical biology* **14**, 23–29 (2010).
7. Shcherbakova, D. M., Subach, O. M. & Verkhusha, V. V. Red fluorescent proteins: advanced imaging applications and future design. *Angew Chem Int Ed Engl* **51**, 10724–10738 (2012).
8. Razansky, D. *et al.* Multispectral opto-acoustic tomography of deep-seated fluorescent proteins in vivo. *Nat Photon* **3**, 412–417 (2009).
9. Weissleder, R. A clearer vision for in vivo imaging. *Nat Biotechnol* **19**, 316–317 (2001).
10. Lin, M. Z. *et al.* Autofluorescent proteins with excitation in the optical window for intravital imaging in mammals. *Chemistry & biology* **16**, 1169–1179 (2009).
11. Strack, R. L. *et al.* A rapidly maturing far-red derivative of DsRed-Express2 for whole-cell labeling. *Biochemistry* **48**, 8279–8281 (2009).
12. Shcherbo, D. *et al.* Near-infrared fluorescent proteins. *Nat Methods* **7**, 827–829 (2010).
13. Morozova, K. S. *et al.* Far-red fluorescent protein excitable with red lasers for flow cytometry and superresolution STED nanoscopy. *Biophysical journal* **99**, L13–15 (2010).
14. Piatkevich, K. D. *et al.* Extended Stokes shift in fluorescent proteins: chromophore-protein interactions in a near-infrared TagRFP675 variant. *Scientific reports* **3**, 1847 (2013).
15. Filonov, G. S. & Verkhusha, V. V. A near-infrared BiFC reporter for in vivo imaging of protein-protein interactions. *Chemistry & biology* **20**, 1078–1086 (2013).
16. Piatkevich, K. D., Subach, F. V. & Verkhusha, V. V. Engineering of bacterial phytochromes for near-infrared imaging, sensing, and light-control in mammals. *Chem Soc Rev* **42**, 3441–3452 (2013).
17. Filonov, G. S. *et al.* Bright and stable near-infrared fluorescent protein for in vivo imaging. *Nat Biotechnol* **29**, 757–761 (2011).
18. Filonov, G. S. *et al.* Deep-tissue photoacoustic tomography of a genetically encoded near-infrared fluorescent probe. *Angew Chem Int Ed Engl* **51**, 1448–1451 (2012).
19. Nedosekin, D. A. *et al.* Synergy of photoacoustic and fluorescence flow cytometry of circulating cells with negative and positive contrasts. *J Biophotonics* **6**, 425–434 (2013).
20. Shcherbakova, D. M. & Verkhusha, V. V. Near-infrared fluorescent proteins for multicolor in vivo imaging. *Nat Methods* **10**, 751–754 (2013).
21. Gamelin, J. *et al.* A real-time photoacoustic tomography system for small animals. *Opt Express* **17**, 10489–10498 (2009).
22. Song, K. H. & Wang, L. V. Deep reflection-mode photoacoustic imaging of biological tissue. *J Biomed Opt* **12**, 060503 (2007).
23. Kedrin, D. *et al.* Intravital imaging of metastatic behavior through a mammary imaging window. *Nat Methods* **5**, 1019–1021 (2008).
24. Xu, Y., Wang, L. V., Ambartsoumian, G. & Kuchment, P. Reconstructions in limited-view thermoacoustic tomography. *Med Phys* **31**, 724–733 (2004).
25. Zhang, H. F., Maslov, K., Stoica, G. & Wang, L. V. Functional photoacoustic microscopy for high-resolution and noninvasive in vivo imaging. *Nat Biotechnol* **24**, 848–851 (2006).
26. Deliolanis, N. C. *et al.* In vivo tomographic imaging of red-shifted fluorescent proteins. *Biomed Opt Express* **2**, 887–900 (2011).
27. Galanzha, E. I. *et al.* Photoacoustic and photothermal cytometry using photoswitchable proteins and nanoparticles with ultrasharp resonances. *J Biophotonics* **7**, in press (2014). doi: 10.1002/jbio.201300140.
28. Maslov, K., Zhang, H. F., Hu, S. & Wang, L. V. Optical-resolution photoacoustic microscopy for in vivo imaging of single capillaries. *Opt Lett* **33**, 929–931 (2008).

Acknowledgments

We thank M. Lin (Stanford University), B. Glick (University of Chicago) and K. Lukyanov (Institute of Bioorganic Chemistry, Russia) for the plasmids encoding the mNeptune, E2-Crimson and eqFP670 proteins, respectively. We thank L. Luecking for assistance with maintaining cell cultures and J. Ballard for help with editing the manuscript. This work was supported by the grants GM073913 and CA164468 (to V.V.V.) and EB016963 and Director's Pioneer Award EB016986 (to L.V.W.) from the National Institutes of Health.

Author contributions

D.M.S. prepared iRFP670 and iRFP720 expressing cells, characterized iRFP670 and iRFP720 expression by means of fluorescent imaging. A.K., J.X. and L.V.W. designed and conducted photoacoustic experiments to image iRFP670 and iRFP720. V.V.V. designed and coordinated the project, and together with D.M.S. and A.K. wrote the manuscript.

Additional information

Supplementary information accompanies this paper at http://www.nature.com/scientificreports

Competing financial interests: L.V.W. has a financial interest in Microphotoacoustics, Inc. and Endra, Inc., which, however, did not support this work.

How to cite this article: Krumholz, A., Shcherbakova, D.M., Xia, J., Wang, L.V. & Verkhusha, V.V. Multicontrast photoacoustic *in vivo* imaging using near-infrared fluorescent proteins. *Sci. Rep.* **4**, 3939; DOI:10.1038/srep03939 (2014).